

Chapter 2

Micro-/Nanointegrated Fabrication Technique for Silicon

Abstract Silicon is one of the most important materials for the development of electronics science and technology, which is the footstone of integrated circuits (IC), electronic communication systems, solar cells, micro-electro-mechanical systems (MEMS), etc. Since the 60s and 70s in the last century, the high-precision fabrication technology based on silicon has been developed rapidly. In the past five decades, Si-based microfabrication technology was developed from two aspects, including bulk processes and surface processes, which has already become a mature technical field. More importantly, bulk processes realize the dream of fabricating 3-D structures at the microscale level. Among all of the bulk processes, deep etching process is one of the most important techniques. Deep reactive-ion etching (DRIE) process is an essential deep etching process, and high-aspect-ratio structures are fabricated by using the alternation of etching steps and passivation steps. DRIE process was also called Bosch process due to the first developer of Bosch company. This chapter presents a micro-/nanointegrated fabrication technique for silicon based on an improved DRIE process, and several Si-based samples with attractive properties are demonstrated.

2.1 Nanoforest Fabrication Based on an Improved DRIE Process

2.1.1 Deep Reactive-Ion Etching (DRIE) Process

Generally, plasma etching processes can be classified into two main types, including reactive-ion etching (RIE) process and deep reactive-ion etching (DRIE) process. Both of these two processes utilize plasma to impact the substrate to realize the etching; however, their working principles are different. RIE process only contains the etching step, and there is only one radio frequency (RF) source to ionize

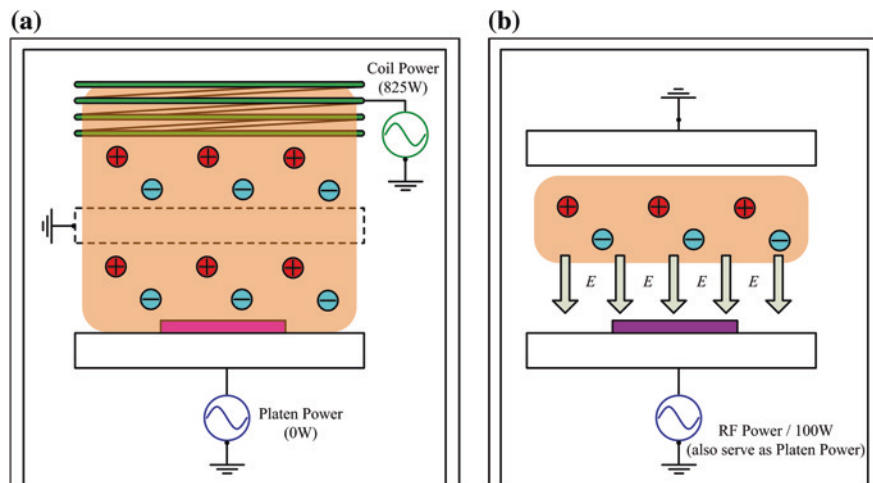


Fig. 2.1 The working principles of **a** deep reactive-ion etching (DRIE) process and **b** reactive-ion etching (RIE) process

the gas molecule and generate the plasma, and this RF source also serves as a platen power to accelerate the ions to impact the substrate. The working principle of RIE is shown in Fig. 2.1a. If neglect the direction influence from the RF source accelerating the plasma, the chemical reaction plays a dominant role in the etching process of plasma treatment on the substrate. And therefore, the etching rate in all directions approximately equals under the ideal condition, i.e., isotropic etching.

DRIE process is a highly anisotropic etching process, and it contains two steps, etching and passivation. Etching step utilizes high-concentration plasma ion to do physical impact and chemical etching, and the passivation step is using another plasma gas to treat the surface and form a polymeric layer by polymerization reactions. The etching step in DRIE process is basically consistent with the RIE etching mechanism, i.e., isotropic etching. However, in the standard DRIE process, etching steps and passivation steps proceed alternately. By using the protection of polymeric layer deposited by passivation steps to the vertical surface, the high-aspect-ratio structure can be realized step by step. And therefore, from the point of view of the final etching result, DRIE process is considered as a highly anisotropic etching process. To realize the above function, DRIE equipment contains two RF sources. One is used to generate the plasma, and the other (i.e., platen power source) is used to control the internal electrical field. The working principle of DRIE is shown in Fig. 2.1b.

According to the above description, it is obvious that DRIE process has better controllability and wider application in the microfabrication field compared with RIE process, due to its two independent RF sources. Based on the method of generating plasma ions, DRIE process equipment has two types, inductively coupled



Fig. 2.2 The ICP equipment applied in the DRIE process

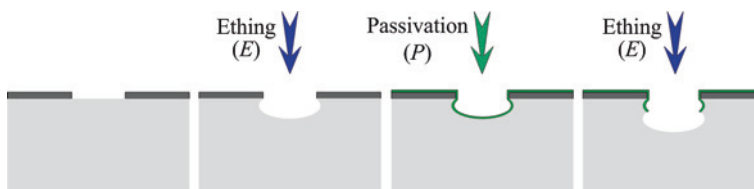


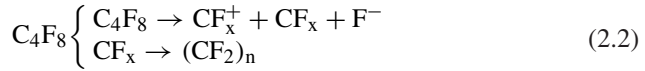
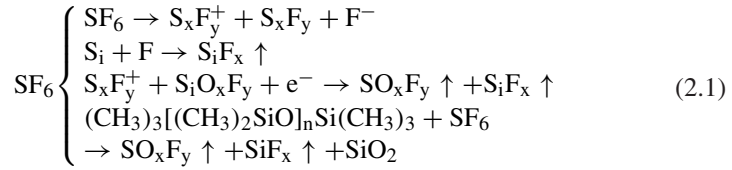
Fig. 2.3 The working principle of standard Bosch DRIE process

plasma (ICP) and capacitance-coupled plasma (CCP). The Multiplex ICP 48443 equipment produced by Surface Technology Systems (STS) Company is a typical one. And in this thesis, we used this equipment as shown in Fig. 2.2 to perform related experiments.

In the standard Bosch DRIE process, two types of gases are alternately used in the reaction chamber to realize the etching and passivation steps, respectively. These gases are formed high-dense plasma ions via glow discharge by RF power. The working principle of standard Bosch DRIE process is shown in Fig. 2.3.

The DRIE process contains complicated physical and chemical reactions. Basically, the etching plasma ions react with Si-based substrate and the formed gas is then released, while the passivation plasma ions form a polymer film on the

surface of Si-based substrate. The chemical reactions are shown in Eqs. (2.1) and (2.2). As a common recipe of using SF_6 (etching gas) and C_4F_8 (passivation gas), the chemical reactions are described as follows.



During etching steps, complicated chemical reactions will happen between etching gas plasma ions and the substrate, and the etching rates in all directions are approximately same, which can be considered as isotropic etching step. However, due to the acceleration of platen power, the etching rate in the vertical direction is larger. During passivation steps, a polymeric thin film is formed via polymerization reactions on the substrate surface resulting in covering and protecting the substrate surface. However, due to the vertical directionality of etching steps, the polymeric film in the horizontal direction can be removed completely, and then, the substrate is further etched downwards, while the polymeric film on the vertical surface cannot be completely removed by etching steps, which protects the substrate in the vertical direction. Consequently, as the continuous alternation of etching steps and passivation steps, the high-dense high-aspect-ratio structure forms onto the substrate. The standard DRIE process is a core top-down technique of bulk silicon microfabrication.

2.1.2 Nanostructuring by an Improved DRIE Process

Based on the standard Bosch DRIE process, we proposed a maskless wafer-level nanofabrication technique based on an improved DRIE process [1–4]. By optimizing the process parameters of DRIE process, the polymer deposited during passivation steps cannot be removed completely. Thus, the residual polymeric nanoparticles serve as self-masks to protect the substrate during the etching steps, which results in high-dense high-aspect-ratio nanopillars. The schematic illustration of the formation of nanostructures by the improved DRIE process is shown in Fig. 2.4a, b shows SEM images of the growth procedure of nanostructures.

Basically, the optimization of DRIE process parameters is enhancing the passivation step or weakening the etching step. By a large amount of comparative experiments with one variable parameter, four key process parameters for the nanostructure formation were determined, i.e., gas flow, platen power, time ratio of etching and passivation (E/P), and total cycles. More importantly, different

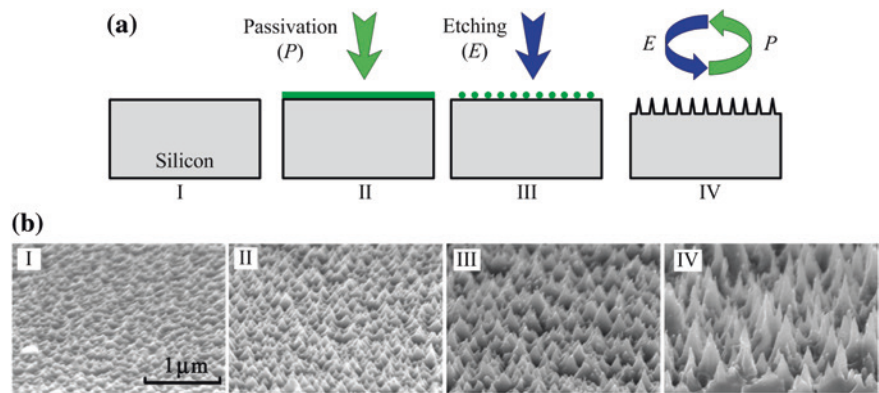


Fig. 2.4 Formation of nanostructures by an improved maskless DRIE process. **a** Schematic illustration. **b** SEM images

Table 2.1 The working ranges of DRIE process

| Type | Gas flow (sccm) | | Time ratio of E/P ^a (s:s) | Platen power (W) | Total cycles |
|-------------------|-----------------|-------------|--------------------------------------|------------------|--------------|
| | Etching | Passivation | | | |
| Normal etching | 100 | 70 | 4/5 | 10 | 16 |
| Hybrid etching | 30 | 50 | 4/5 | 10 | 80 |
| Etching stop | 30 | 50 | 4/5 | 5 | 16 |
| | 30 | 50 | 4/5 | 6 | 40 |
| Nanopillar forest | 30 | 50 | 4/5 | 8 | 40 |

^aE/P refers to etching/passivation

working ranges (i.e., fabrication results) of DRIE process were observed by the combinations of the above key parameters, as shown in Table 2.1.

Lots of comparative experiments show that the formation of nanostructures tightly correlates with the gas flow, which directly determines the working range of DRIE process. While other parameters, including total cycles, platen power, and E/P, have the significant influence on the profile of nanostructures. In summary, the gas flow controls the DRIE working range, while the other three parameters realize the controllable formation of nanopillar forest.

2.1.3 Mechanism of Controllable Formation of Nanostructures

Controllability is one of the key factors to assess whether a fabrication technique has an attractive application future. As mentioned in Sect. 2.1.2, the profile of nanostructures can be controlled by adjusting E/P, total cycles, and platen power.

As shown in Fig. 2.4b, although the fabricated nanostructures are non-uniform, the statistics data of their geometries are highly consistent in the large area. Thus, in order to better characterize and analyze the fabrication results, all the structural parameters are the average data in a unit area of $5\ \mu\text{m} \times 5\ \mu\text{m}$ in the following discussion. According to the optical test and the wettability characterization, although the individual nanostructures are non-uniform, but the properties of fabricated samples are determined by the statistical data of nanopillars in a certain area, i.e., average structural data.

The profile of nanostructures can be defined by aspect ratio (AR) and density, where AR means the ratio of height (h) to diameter (d) at the half-height position, i.e., $AR = h/d$, and the density refers to the space (s) of adjacent nanopillars, as shown in Fig. 2.5. According to the comparative experiments, the density is extremely sensitive to the gas flow, and the optimal high-dense nanostructures (i.e., $s = 100\text{--}400\ \text{nm}$) can only be obtained when the flows of etching gas and passivation gas are set as 30 sccm and 50 sccm, respectively. Besides, the quantitative relations between AR and the other three process parameters, i.e., E/P, total cycles, and platen power, are shown in Fig. 2.6.

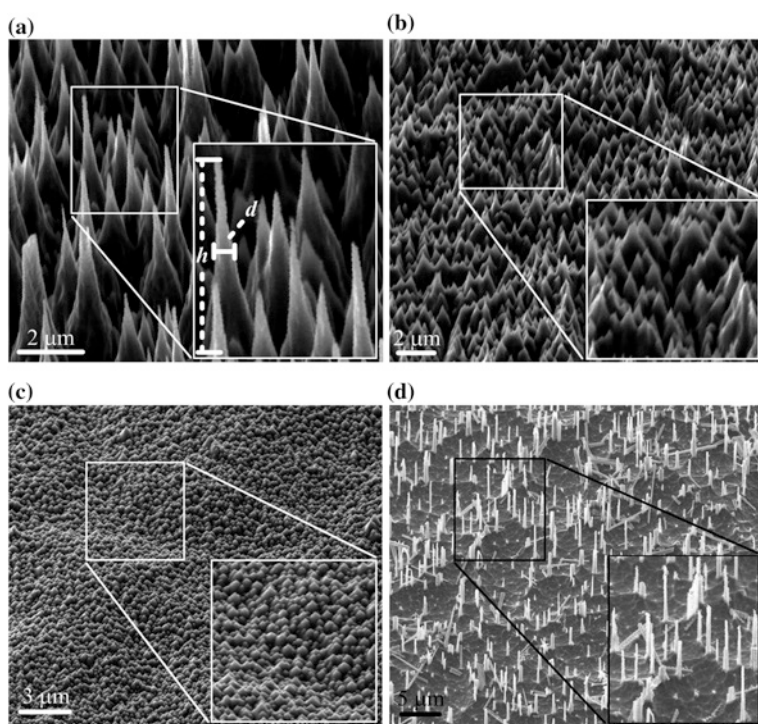


Fig. 2.5 Different types of nanoscale surfaces. **a** High-dense high-aspect-ratio nanostructures (space: 100–400 nm, AR : 8:1–13:1). **b** High-dense medium-aspect-ratio (space: 100–400 nm, AR : 3:1–7:1). **c** High-dense low-aspect-ratio (space: 100–400 nm, AR : 1:1–2:1). **d** Low-dense high-aspect-ratio (space: 1–10 μm , AR : 8:1–13:1)

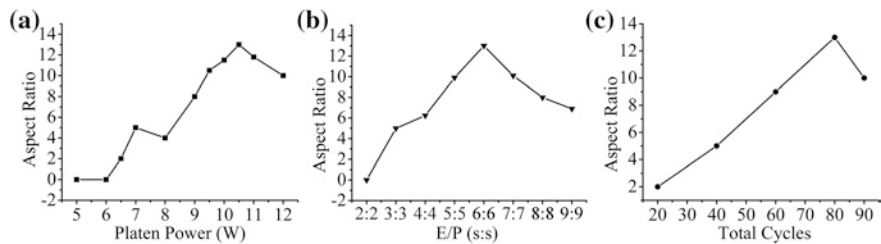


Fig. 2.6 The effects of key process parameters on the aspect ratio of nanostructures

Fig. 2.7 The fabricated 4-in. wafer-level sample



The curves in Fig. 2.6 reveal single-peak distribution, and in general, the curves tend to increase to a maximum value and then decrease from that point. The maximum ARs appear at platen power of 10.5 W, E/P of 6s:6s, and total cycles of 80. This trend is due to the overetching phenomenon. After AR reaches the maximum point, the further etching will reduce the height of nanopillar and then lower its AR. Based on this improved DRIE process, nanostructures with different profiles can be fabricated onto the substrate by quantitatively adjusting the process parameters. As shown in Fig. 2.5, four different nanostructures were realized: (a) high-dense high-aspect-ratio type, (b) high-dense medium-aspect-ratio type, (c) high-dense low-aspect-ratio type, and (d) low-dense high-aspect-ratio type. More importantly, this novel fabrication technique can be used to realize nanostructures onto the wafer-level substrate shown in Fig. 2.7, which shows the attractive ability of large-scale mass production.

2.2 Fabrication of Si-based Micro-/Nanohierarchical Structures

Based on the combination of traditional microfabrication techniques and the improved DRIE process for maskless nanofabrication, we can realize the Si-based micro-/nanohierarchical structures. As mentioned above, this new nanofabrication approach is maskless, simple, controllable, cost-efficient and mass production, compared with traditional nanofabrication methods.

2.2.1 Structural Design

Microstructures show various types and geometries corresponding to different application fields. However, the microstructure with periodic arrays is one of the most important types, which is essential in many fields. Besides, the micro-/nanostructures with periodic arrays is an effective method to test the reliability and homogeneity of this new micro-/nanointegrated fabrication technique. Here, in order to extend the application fields of this work, we selected two typical microstructures with inverted pyramid arrays and V-shaped-groove arrays, respectively, as shown in Fig. 2.8. The microstructure with inverted pyramid arrays is widely used in the optical field, and one typical application is serving as the light-trapping structure for high-performance solar cells. The microstructure with V-shaped-groove arrays is widely used in the biomedical field, such as constructing microchannels for microfluidic chips.

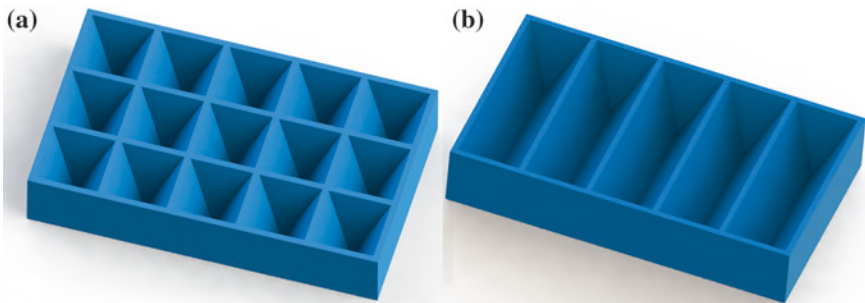


Fig. 2.8 Two types of Si-based microstructures for fabricating micro-/nanohierarchical structures. **a** Inverted pyramid arrays. **b** V-shaped-groove arrays

2.2.2 Fabrication Process

The fabrication process of micro-/nanohierarchical structures (i.e., micro-/nanodual-scale structures) basically contains two steps, i.e., microstructure fabrication and nanostructure fabrication. First, the traditional microfabrication technique is employed to realize microstructures, including photolithography and wet etching. Second, the improved DRIE process proposed above is used to form nanostructures atop microstructures. The fabrication process flow of Si-based micro-/nanohierarchical structures based on the improved DRIE process is shown in Fig. 2.9.

An N-type (100) 4-in. silicon substrate was used, whose thickness is 525 μm and the resistivity is 2–4 $\Omega\text{ cm}$. First, the silicon substrate was immersed in a 30 % HF solution for one minute to remove the oxidation layer. Then, a $\sim 2000\text{ \AA}$ Si_3N_4 layer was deposited on the silicon substrate by low-pressure chemical vapor deposition (LPCVD) process, as shown in Fig. 2.9a. Then, the Si_3N_4 layer was patterned by photolithography and reactive-ion etching (RIE) process, as shown in Fig. 2.9b. To form well-designed microstructures (i.e., inverted pyramid arrays and V-shaped-groove arrays with cross-sectional views of inverted triangle or trapezoid), KOH wet etching process was performed at 85 $^\circ\text{C}$ as shown in Fig. 2.9c, followed by removal of Si_3N_4 layer by RIE as shown in Fig. 2.9d. Finally, high-dense high-aspect-ratio nanostructures were formed atop microstructures by an inductively coupled plasma (ICP) etcher using the improved DRIE process. To better describe the advantages of this novel Si-based micro-/nanointegrated

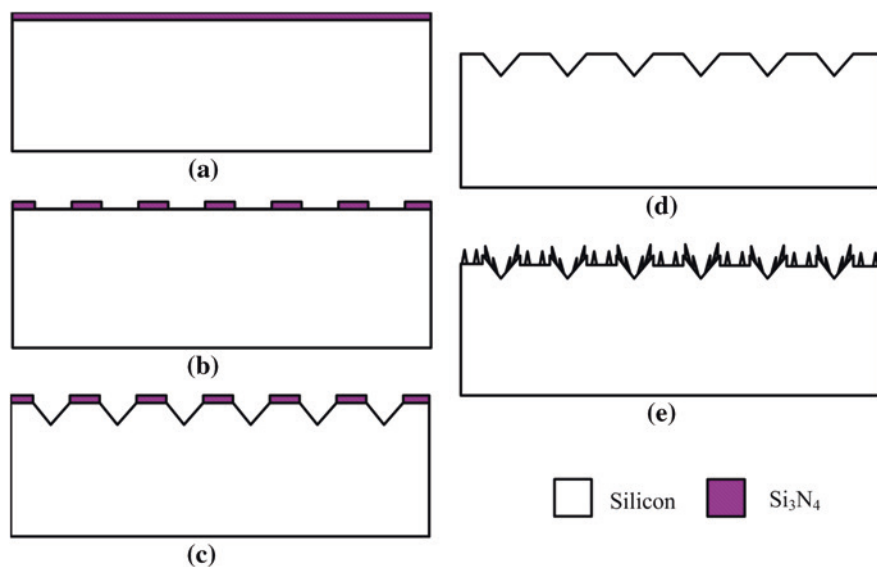


Fig. 2.9 Schematic view of the fabrication process flow of Si-based micro-/nanohierarchical structures based on the improved DRIE process

fabrication technique, we decompose the process in Fig. 2.9e and the detailed illustration of producing nanostructures atop microstructures based on the improved DRIE process is shown in Fig. 2.10.

Figures 2.11 and 2.12 show the SEM images of two types of fabricated Si-based microstructures and micro-/nanohierarchical structures. Figures 2.11I and 2.12I show the morphology of microstructures, i.e., the fabrication result shown in

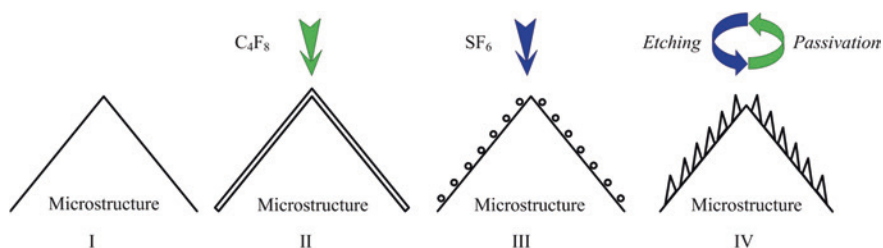


Fig. 2.10 Schematic illustration of producing nanostructures atop microstructures based on optimized DRIE process

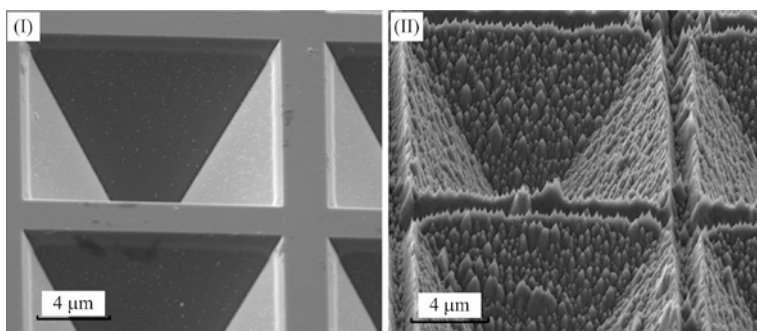


Fig. 2.11 SEM images of (I) microstructures and (II) micro-/nanohierarchical structures with inverted pyramid arrays

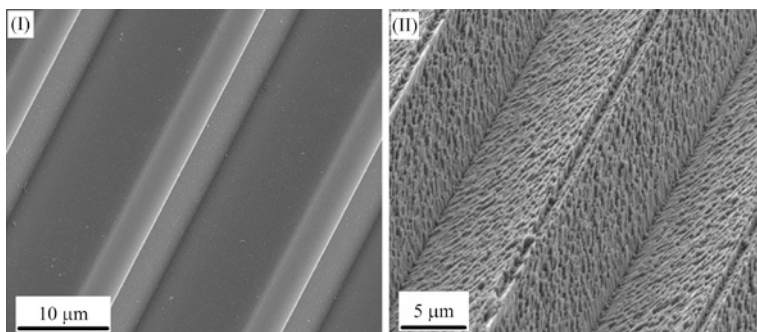


Fig. 2.12 SEM images of (I) microstructures and (II) micro-/nanohierarchical structures with V-shaped-groove arrays

the Figs. 2.9d, 2.11II and 2.12II shows the micro-/nanohierarchical structures, i.e., the fabrication result as shown in Fig. 2.9e.

2.2.3 Characterization and Analysis of Micro-/NanoHierarchical Structures

In this subsection, all the characterizations of fabricated samples were performed by using scanning electron microscope (Quanta 600F, EFI Company). Figure 2.13 shows the SEM images of fabricated Si-based micro-/nanohierarchical structures. Clearly, according to the top-view image, periodic microstructures are completely covered by nanostructures, even on the inclined surfaces with a title angle of 54.74° shown in Figs. 2.13 and 2.14.

Figure 2.15 shows the SEM images of large-scale micro-/nanohierarchical structures. The fabricated MNHS samples clearly show the perfect uniformity, even at wafer-scale level, which demonstrates the reliability of the presented Si-based micro-/nanointegrated fabrication technique. Regardless of doping type, resistance, and thickness of Si substrates, the fabrication results keep highly consistent. Besides, the periodic microstructures with different dimensions were designed (shown in Table 2.2), and all the SEM images show that microstructures are well covered by nanostructures completely.

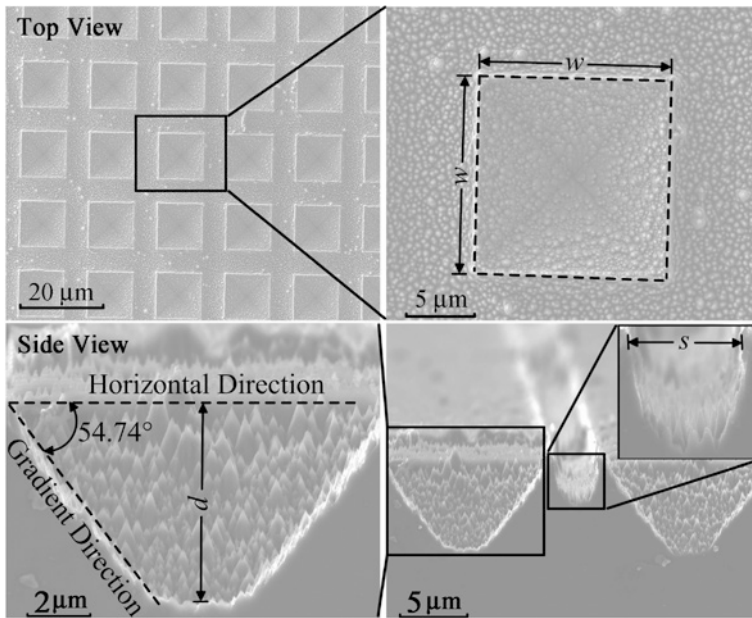


Fig. 2.13 SEM images of Si-based micro-/nanohierarchical structures from top view (*upper*) and cross-sectional view (*lower*)

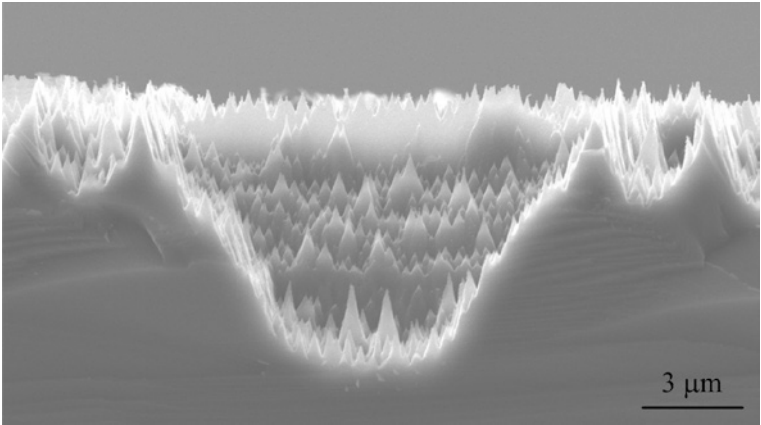


Fig. 2.14 SEM images of Si-based micro-/nanohierarchical structures from cross-sectional view

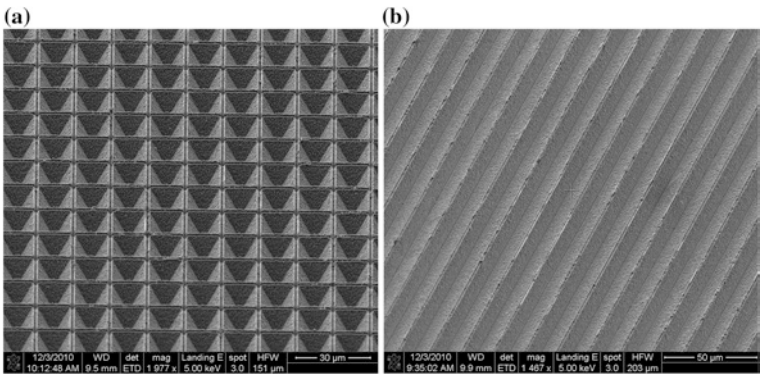


Fig. 2.15 SEM images of large-scale Si-based micro-/nanohierarchical structures. **a** Pyramid-shaped MNHS **b** Groove-shaped MNHS

Table 2.2 Structural parameters of micro-/nanohierarchical structures

| Type and No. | | Structural parameters | | |
|-------------------|---------------------------------|-----------------------|-------------|------------|
| | | Width (μm) | Space (μm) | Depth (μm) |
| Inverted pyramids | P ₁ ~ P ₇ | 10, 13, 15, 19 | 2, 4, 8, 16 | 4.4 |
| V-shaped grooves | G ₁ ~ G ₅ | 10, 13, 15 | 2, 4, 6 | 13.4 |

We can realize the microstructures with inverted trapezoids by controlling the KOH etching time shown in Fig. 2.9c and can further realize the micro-/nanohierarchical structures with the cross-sectional view of inverted trapezoid shown in Fig. 2.16. This also validates the universality of this fabrication technique. As mentioned above, regardless of doping type, resistance, and thickness of

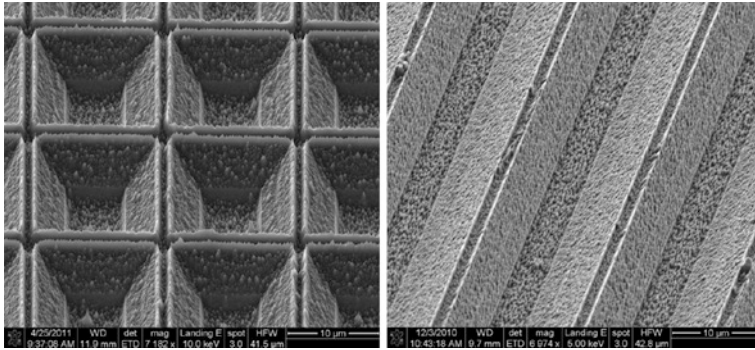


Fig. 2.16 SEM images of Si-based micro-/nanohierarchical structures with the cross-sectional view of inverted trapezoid

Si substrates and regardless of profiles and sizes of microstructures on the surface, this Si-based micro-/nanointegrated fabrication technique based on the improved DRIE process is repeatable, controllable, cost-efficient, and reliable.

2.3 Interaction of Multiscale Structures Based on Silicon

Due to the combination of multiscale structures, more factors have to be considered in the fabrication procedure, and the related chemical–physical energy transfer becomes more complicated, i.e., the combination of multiscale structures brings some new challenges and phenomena, which are an essential research field of micro-/nanointegrated fabrication. However, there is a lack of knowledge considering multiscale interaction because of size effect, controllability, and repeatability.

In order to investigate the interaction of structures at different scales, the microstructures are specifically designed to be inverted pyramids and V-shaped grooves, and each type contains two cross sections with inverted triangle and trapezoid, respectively, shown in Figs. 2.11, 2.12, 2.15 and 2.16. For different micro-/nanohierarchical structures, their basic unit can be classified into two types, horizontal and inclined surfaces, as shown in Fig. 2.17, where the solid line and the dash line show the profile of microstructures and MNHS, respectively.

During the MNHS fabrication, the etching rate on the horizontal surface is faster than that on the inclined surface, as shown in Fig. 2.18. In the fixed process time of t , the depth change of horizontal surfaces is set as ΔH and that of inclined surfaces is set as Δh , thus $\Delta H > \Delta h$ according to Figs. 2.14, 2.17 and 2.18. And there is a quantitative relation as follows:

$$\Delta H(= \Delta h + \Delta d) > \Delta h \quad (2.3)$$

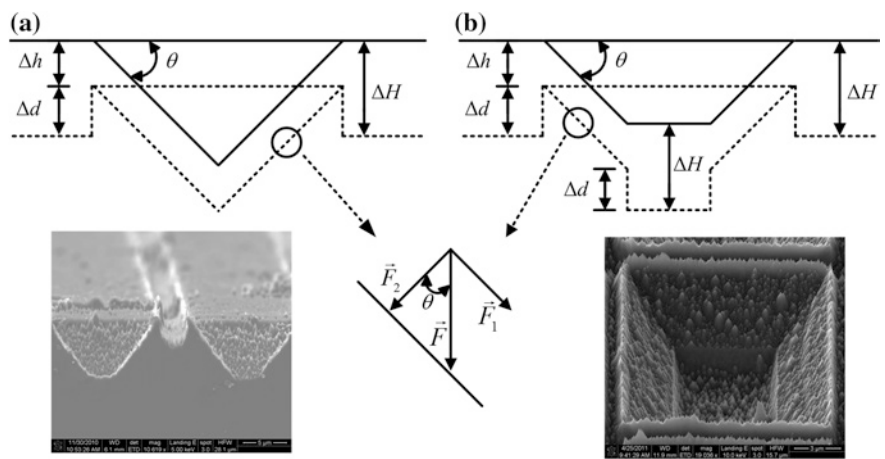


Fig. 2.17 Illustration of the formation of micro-/nanohierarchical structures (*solid line* the profile of microstructure; *dash line* the profile of MNHS). **a** Triangle cross section. **b** Trapezoid cross section

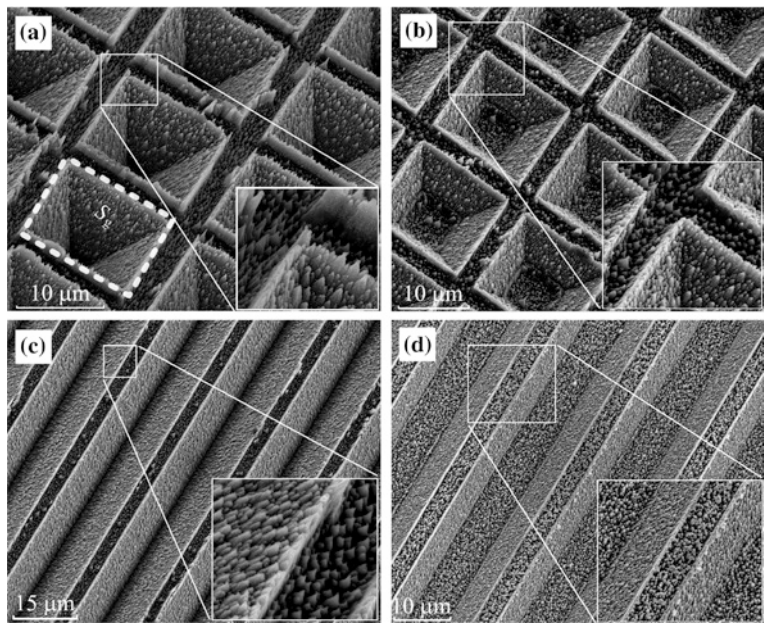


Fig. 2.18 SEM images of Si-based micro-/nanohierarchical structures covered by a thin gold layer

By defining the corresponding average etching velocities $V_h = \Delta H/t$ and $V_i = \Delta h/t$, we can conclude the following relation with the same etching time.

$$V_h > V_i \quad (2.4)$$

The above difference can be attributed to energy flux vector field of plasma ions. There are two RF sources with one controlling the direction of electric field. When the platen power is fixed, the energy flux vector field of ion beam F in the vertical direction will keep constant. The F , whose direction is normal to the horizontal surfaces, can be decomposed into two orthogonal components, i.e., F_1 and F_2 , which are parallel and normal to the inclined surface, respectively, as shown in Fig. 2.18.

$$F_1 = F \times \sin\theta \quad (2.5)$$

$$F_2 = F \times \cos\theta \quad (2.6)$$

And therefore, the etching velocity on the inclined surface is smaller than that on the horizontal surface due to $F_2 < F$. Moreover, the inclined angle θ is approximately constant with the value of 54.74° during the formation of MNHS. Therefore, the relation between V_h and V_i exists as follows:

$$V_h = f(V_i, \theta) \quad (2.7)$$

We have investigated the dual-scale coupling effect during the formation of MNHS above, and the morphology of MNHS also significantly affects the further fabrication. To explore this coupling effect in the multiscale structures, we fabricated Si-based MNHS covered by a thin gold layer of $\sim 500 \text{ \AA}$ by sputtering process, as shown in Fig. 2.18. The surface of Si-based micro-/nanohierarchical structures in Fig. 2.18 presents regular bright and dark areas with the bright on the inclined surface and the dark on the horizontal surface and at the bottom of grooves. To better illustrate these phenomena, Fig. 2.19 gives SEM images of part-enlarged view.

According to the SEM images of micro-/nanomultiscale structures shown in Fig. 2.19, gold particles can only be sputtered on inclined surfaces (i.e., C zone). In other words, there are no gold particles on horizontal surfaces (i.e., A zone) and at the bottom of microstructures (i.e., B zone). We believe that two reasons result in these phenomena. First, the dissymmetrical nanostructures atop inclined surfaces are more favorable to capture sputtered gold particles due to the sharper sidewall, which is almost parallel to the incident particles and can reduce the probability of particle rebound. Second, the surface substances on the nanostructures in the C zone are different from those in the A/B zones due to the difference in the energy flux vector field of ion beams and the electric field influence of small-size microstructures during the formation of nanostructures onto microstructures. As for the electric field influence of small-size microstructures, these phenomena become less obvious when the size of the microstructures gradually increase, as shown in Fig. 2.18d.

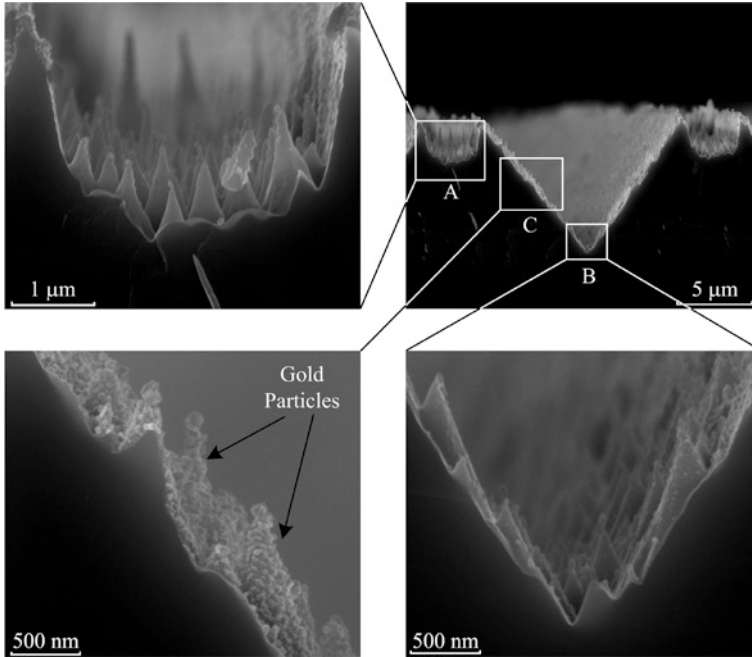


Fig. 2.19 SEM images of cross-sectional view of Si-based MNHS covered by a gold layer

2.4 Properties of Si-Based Micro-/NanoHierarchical Structures

Si-based materials have widespread use for optical devices and photoelectric converters; however, the high reflectance hampers their further development. Increasing the roughness has been proven as an effective method to reduce the reflectance, and thus, Si-based MNHS combining periodic microstructures and high-dense nanostructures can greatly lower the reflectance, which is very useful for improving the sensitivity and photoelectric conversion efficiency of Si-based optical devices. Besides, such a multiscale combination also significantly maximizes the surface area and minimizes the solid–liquid contact area of a water droplet on the surface, thus improving the super-hydrophobic property. Moreover, due to using C_4F_8 as the passivation gas for DRIE process, the fluorocarbon polymer residues on the Si substrate surface will significantly reduce the surface energy and further strengthen the super-hydrophobicity. Thus, this subsection is to introduce two excellent properties of Si-based MNHS, i.e., wide-band anti-reflectance and super-hydrophobicity.

2.4.1 Anti-reflective Property

The roughness of micro-/nanohierarchical structures is greatly improved due to the combination of microstructures and nanostructures. Therefore, when light is incident on the dual-scale surface, the incident light is repeatedly reflected and refracted, thus realizing the anti-reflectance. Figure 2.20 shows the reflectance measurement results among samples including micro-/nanohierarchical structures (MNHS), black silicon (BS), and microstructures (MS) under an incidence angle of 6° using Lambda 950 spectrophotometer (Perkin Elmer Inc.). Clearly, with the same DRIE process parameters, the reflectance order is as follows:

$$R_{\text{MNHS}} < R_{\text{BS}} < R_{\text{MS}} \quad (2.8)$$

Compared with flat silicon substrate, pure microstructures have lower optical reflectance but still high ($R > 30\%$). The reflectance of pure microstructures increases as the wavelength of incident light decreases and is higher than 5% in the visible range. Pure nanostructures have good wideband anti-reflectance, and the reflectance decreases to 1% in the measurement range. And MNHSs further reduce the reflectance. The reflectance of MNHSs without any reflective coating has been reduced to less than 0.6% in a wavelength range from 200 to 2500 nm , and correspondingly, the optimized size parameters, i.e., width = $13\text{ }\mu\text{m}$ and space = $4\text{ }\mu\text{m}$, are obtained. Besides, MNHS with inverted pyramids exhibit lower reflectance than with V-shaped grooves, due to the more dense array structures of the former.

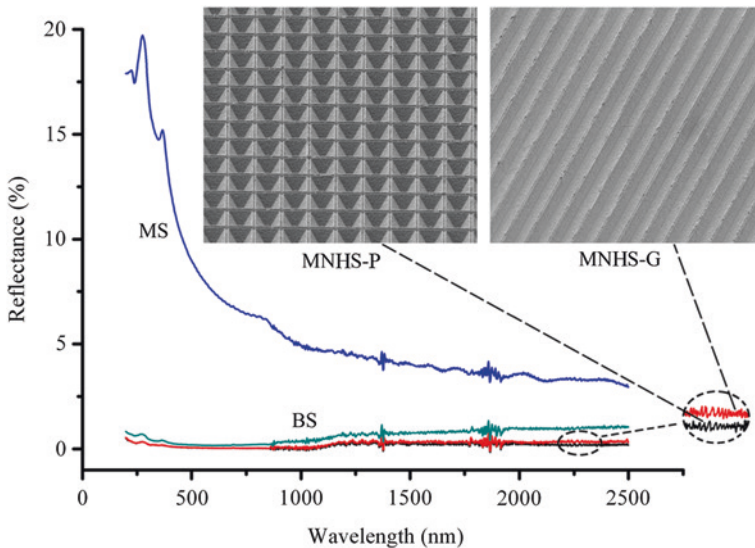


Fig. 2.20 Comparison of reflectance among MNHSs with inverted pyramids and V-shaped grooves under an incidence angle of 6° . *BS* black silicon; *MS* microstructures; *MNHS-P* MNHS with inverted pyramids; *MNHS-G* MNHS with V-shaped grooves

For the rough surfaces, pure reflectance test does not accurately reflect the true anti-reflective effect due to the presence of the scattering phenomena. Therefore, we further measured hemispherical reflectance of fabricated samples, i.e., the sum of reflectance (R) and scattering (S), shown by dash line in Fig. 2.21. The hemispherical reflectance results indicate the same trend as pure reflectance results. The MNHS have the best anti-reflectance property with hemispherical reflectance lower than 5 %. Compared with the polished normal silicon surface, whose hemispherical reflectance is larger than 35 %, the MNHSs have suppressed the hemispherical reflectance by a factor of >85.7 %, showing a highly effective optical absorption characteristics.

To comprehensively test the optical properties of MNHS samples, we also investigated their optical absorption (A). The optical absorption can be calculated according to the following equation,

$$A = 100 \% - R - S - T \quad (2.9)$$

where A denotes absorption, R denotes reflectance, S denotes scattering, and T denotes transmittance.

As mentioned above, the hemispherical reflectance is the sum of R and S . That is to say, after measuring the hemispherical reflectance and the transmittance, the optical absorption can be directly obtained, as indicated by the solid line in Fig. 2.21. The MNHSs can absorb ~95 % incident light during the whole solar spectrum (i.e., 400–1000 nm), making them an excellent optical materials.

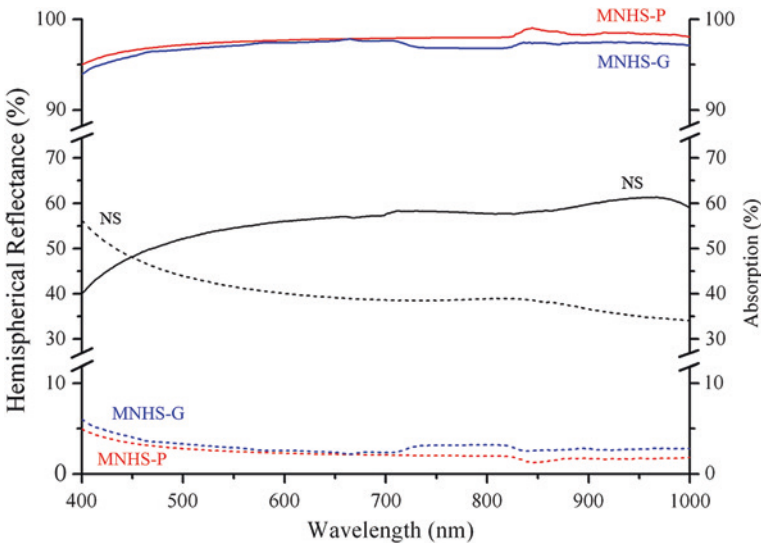


Fig. 2.21 Hemispherical reflectance spectrums (*dash lines*) and absorption spectrums (*solid lines*) of optimized MNHS. NS normal silicon; MNHS micro-/nanodual-scale structure (MNHS-P MNHS with inverted pyramids; MNHS-G MNHS with V-shaped-groove arrays)

For pure microstructures without nanostructures, their optical properties are sensitive to their structural parameters. Therefore, the structural optimization and accurate fabrication are the key for their applications in the optical field, but in the meantime, this also leads to their reliability descending and cost increasing. The inclined surfaces of microstructures can effectively reflect the incident light repeatedly, thus resulting in the high optical absorption. While most of the incident light on the horizontal surface will be directly reflected out and wasted. And therefore, the ratio of surface area in the horizontal direction to the total surface area on a sample, which is defined as *RSA*, qualitatively determines the quality of its optical property. That is to say, the larger the *RSA*, the higher the hemispherical reflectance; the smaller the *RSA*, the lower the hemispherical reflectance. For pure microstructures, in order to achieve the most excellent anti-reflectance property, the *RSA* value needs to be further reduced. However, the minimum value of *RSA* is restricted by the minimum width of photolithography. Let us take Figs. 2.11 and 2.12 as examples, the space between two adjacent microstructures is determined and limited by the minimal line width of photolithography. The micro-/nanohierarchical structures can be employed to overcome this drawback due to the combination of wideband anti-reflective nanostructures with underlying microstructures.

As shown in Figs. 2.13 and 2.18, to facilitate illustration and understanding, we define the area of a single inverted pyramid or groove as S_g and assume that there are n -inverted pyramids/grooves on the whole sample. Then, we can calculate *RSA* based on the following equation:

$$RSA = (S_{\text{total}} - n \times S_g) / S_{\text{total}} \quad (2.10)$$

where S_{total} is $2 \text{ cm} \times 2 \text{ cm}$. The hemispherical reflectance of MNHS was measured by a UV-3600 spectrophotometer (SHIMADZU Corporation), and the results are shown in Fig. 2.22. Clearly, the hemispherical reflectance of pure microstructures increases from 13.2 to 24 % as the *RSA* increases from 41.6 to 61.7 %. In contrast, the hemispherical reflectance variation of MNHS is limited to less than 2 %, although the *RSA* changes during a wide range from 13.4 to 79.9 %. These results show that the hemispherical reflectance of MNHS is very stable even though the structural parameters vary a lot. Therefore, the optical reflectance of MNHS is not sensitive to structural parameters, which makes it more tolerant toward process errors and solves the mentioned limitation of photolithography.

2.4.2 Super-hydrophobic Property

Hydrophobic materials have attracted much attention in the past decades due to the widespread applications in the industry production and the fundamental research [5, 6]. The hydrophobicity of low-surface-energy materials can be enhanced by surface roughening [7, 8]. Nanostructures, such as nanoporous, nanowires, and nanopillars, have been used to roughen the surfaces and side walls

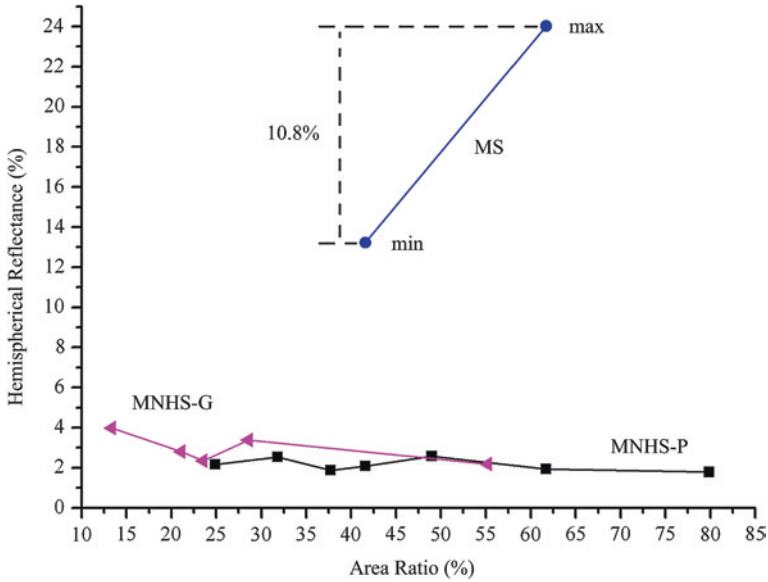


Fig. 2.22 Relation between the hemispherical reflectance and the surface area ratio (RSA) of horizontal surface to the total surface under an incidence wavelength of 700 nm. *MS* pure micro-structure; *MNHS-P* MNHS with inverted pyramids; *MNHS-G* MNHS with V-shaped grooves

of hydrophobic materials to realize the super-hydrophobicity [9, 10]. Although several fabrication methods have been proposed to realize the nanostructures on the microstructures, they are limited by some problems more or less, such as requiring mask, containing several steps, disability in fabricating nanostructures on side walls and low efficiency, as mentioned in Sect. 2.1.2.

While the improved DRIE process for micro-/nanohierarchical fabrication shows its unique properties, such as maskless, wafer level, and mass production, to respond the above problems, the fluorocarbon polymer deposited by passivation steps significantly reduces the surface energy of silicon substrate and thus further strengthens the wettability and realizing the super-hydrophobicity with contact angle (CA) larger than 150° and rolling angle (RA) less than 1° . Here, the static CA was measured by using OCA20 video-based contact angle meter (DataPhysics Instruments GmbH), and other liquid dynamics properties were measured by using JC2000D contact angle meter (POWEEACH).

Figure 2.23 shows the contact angle measurement results of Si-based micro-/nanohierarchical structures. Pyramid-shaped MNHS (MNHS-P) samples with cross sections of inverted triangle and trapezoid are shown in Fig. 2.23a, b, respectively, and groove-shaped MNHS (MNHS-G) samples with cross sections of inverted triangle and trapezoid are shown in Fig. 2.23c, d, respectively. Generally, MNHS-P samples achieve higher CAs than those of MNHS-G samples. Meanwhile, the sample with inverted-triangle cross section exhibits higher CA than that with trapezoid cross section. With optimal structural parameters

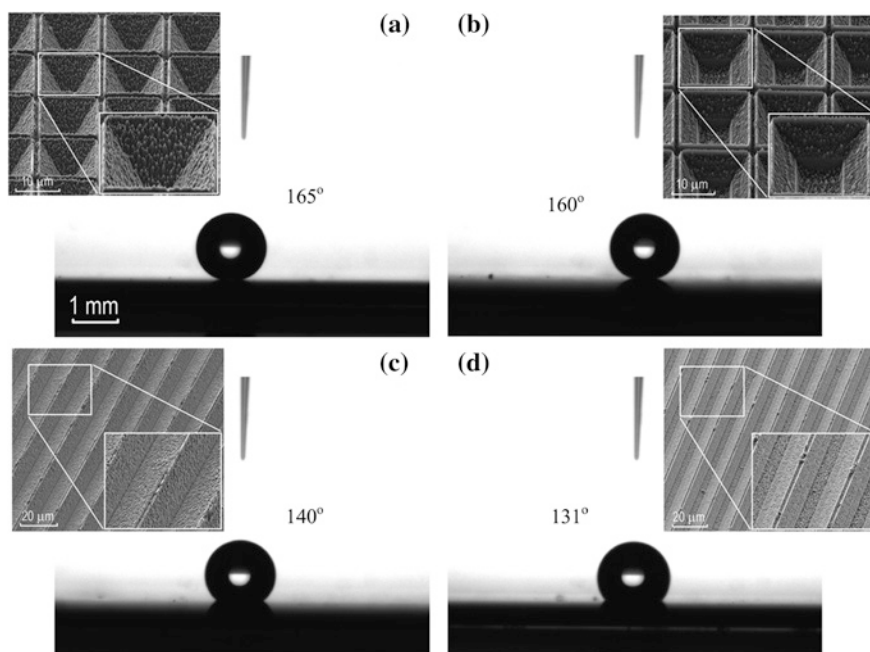


Fig. 2.23 Measurement results of static contact angles of Si-based micro-/nanohierarchical structures (water droplet volume = 2 μL): **a** $\sim 165^\circ$; **b** $\sim 160^\circ$; **c** $\sim 140^\circ$; **d** $\sim 131^\circ$

(i.e., $w = 13 \mu\text{m}$, $s = 2 \mu\text{m}$, and $d = 9.2 \mu\text{m}$), the MNHS-P with inverted-triangle cross section achieved the largest CA of 165° , as shown in Fig. 2.23a.

We further measured the rolling angle, which also characterizes the sample's hydrophobicity. The sample was placed on a flat platform with an inclined angle of below 1° , and a $10 \mu\text{L}$ water droplet was dropped on the sample surface and then freely rolled along the surface, shown in Fig. 2.24. Therefore, the RA of optimized MNHS is below 1° . According to published literatures, the Cassie's model can be used to describe the wettability of the material with ultra-large CA and extreme-small RA. Furthermore, ultra-large CA and extreme-small RA make these MNHS very useful for super-hydrophobic applications, especially to realize the self-cleaning surface. When the rain drops on these MNHS surfaces, it will flow away and take dusts and particles away.

The above CA and RA measurement results confirmed the excellent super-hydrophobic property of Si-based MNHS. As is known, the reliability and stability of super-hydrophobic materials are very important for the practical applications. We further performed squeezing and impact tests to verify the reliability and stability of the super-hydrophobicity of MNHS, as shown in Figs. 2.25 and 2.26. A $10 \mu\text{L}$ water droplet suspended on the tip of an injector, while the fabricated sample touched and squeezed the droplet. Sequentially, the sample descended and departed from the droplet, but the water droplet still suspended on the tip, shown

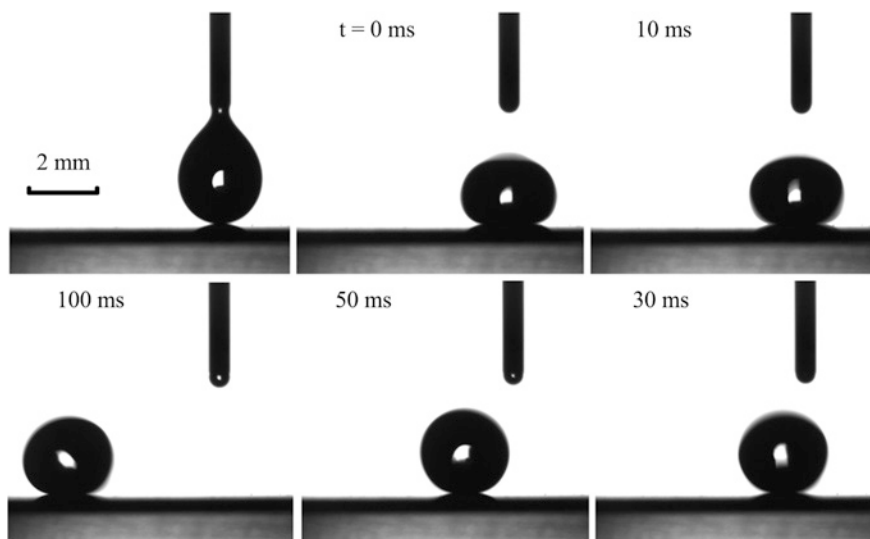


Fig. 2.24 Sequential images of a water droplet (volume = 10 μL) sliding on the MNHS sample with a tilted angle of below 1°

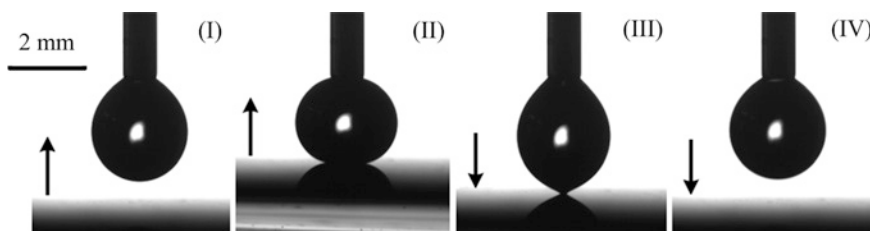


Fig. 2.25 Sequential images of squeezing test (water droplet volume = 10 μL)

in Fig. 2.25. This shows the interface force between the sample and the water droplet is very weak, which validates the stability of the super-hydrophobicity of MNHS.

In Fig. 2.26, a 15 μL water droplet dropped from a height of 5 mm with initial speed of 0 m/s and then impacted the surface of MNHS. According to the sequential images at the 20, 40, 70, 120, and 160 ms, the water droplet bounced for 4–5 times until the potential energy was completely consumed by the friction and water internal flow. In the whole impact procedure, the water droplet did not adhere to the sample surface, demonstrating the reliability of super-hydrophobicity of MNHS. It is worth mentioning that the above reliability and stability tests were carried out three months after the samples were fabricated, which further proves the long-term stability of the super-hydrophobicity of MNHS.

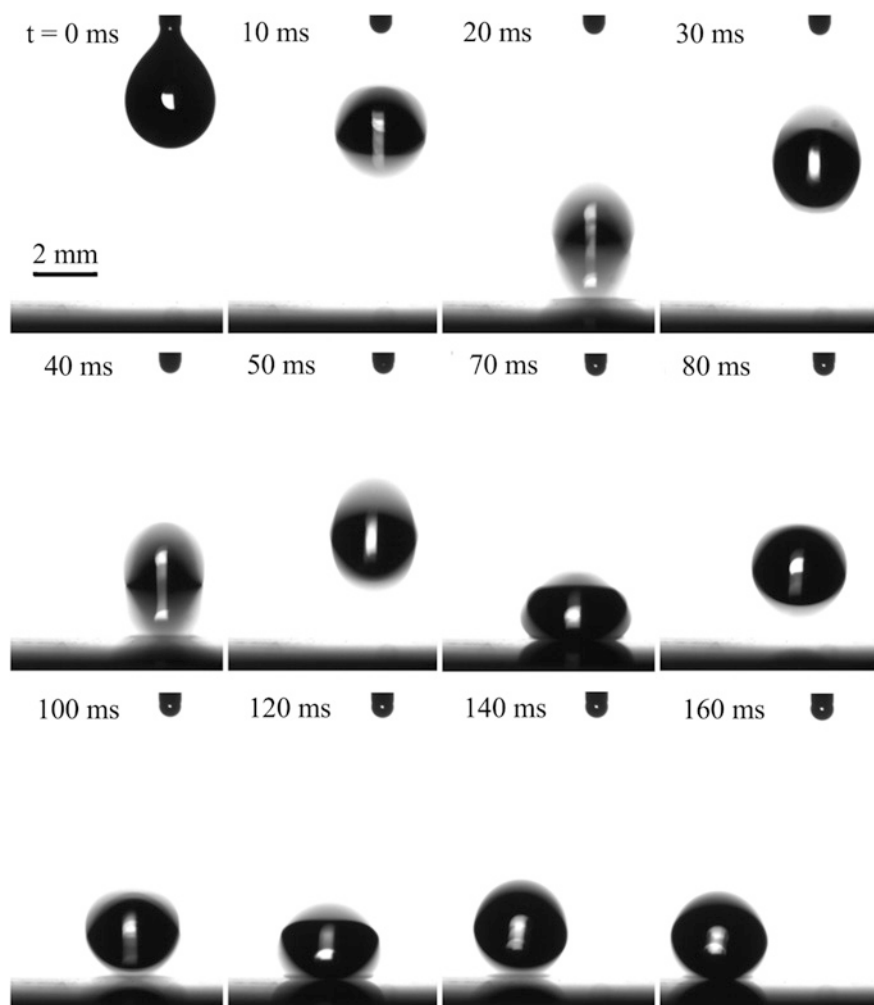


Fig. 2.26 Sequential images of a water droplet (volume = 15 μL) impacting the MNHS sample

Electrowetting is an important and useful property for hydrophobic materials in many applications, such as display devices [11–13]. However, in other fields, e.g., electricity-driven micro-/nanofluids, the reliable super-hydrophobicity in the high voltage is essential. Combining a Picoammeter/Voltage Source (6487, Keithley Instruments Inc.) with the contact angle meter, we investigated the electrowetting property of MNHS by plotting the curve of contact angle versus applied voltage with a 10 μL water droplet, shown in Fig. 2.27. Obviously, the contact angle of MNHS is kept constant at 158° during the voltage increasing from 0 to 300 V, while it decreases to 143° and 115° under the voltage of 350 and 400 V, respectively. And therefore, the electrowetting threshold voltage of the fabricated MNHS

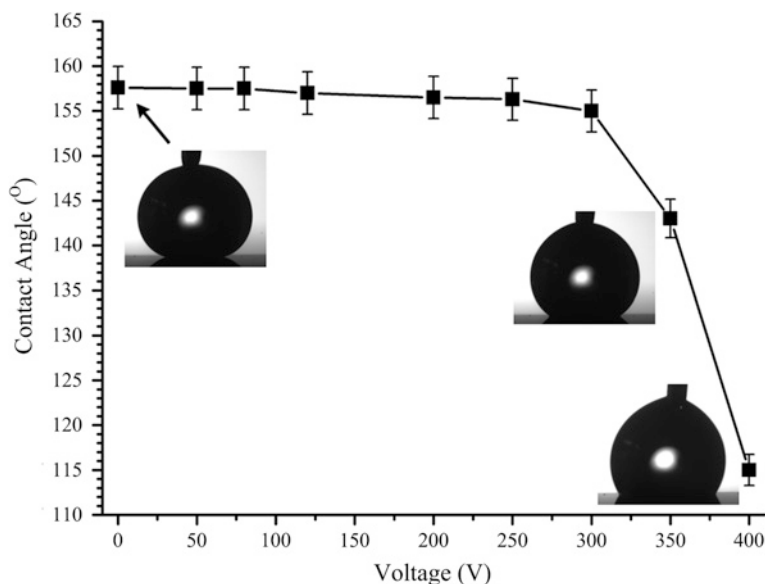


Fig. 2.27 Contact angle of water droplet on the surface of micro-/nanohierarchical structures versus applied voltage (water droplet volume = 10 μL)

is ~ 300 V, higher than that of normal electrowetting materials (below 200 V). In one word, the fabricated MNHS samples based on the optimized DRIE process showed a stable super-hydrophobic property.

2.5 Conclusions

In this chapter, by optimizing process parameters, we propose a maskless nanofabrication method based on an improved DRIE process. Four working ranges of DRIE process were figured out by lots of independent and comparative experiments. The subsequent experiments are carried out to study the key process parameters of DRIE process and their qualitative and quantitative effects on the profile of nanostructures. Finally, a maskless nanofabrication process for silicon is successfully developed, which shows advantages of controllability, large-scale, reliability, and repeatability. By combining traditional microfabrication techniques, we propose a novel micro-/nanointegrated fabrication technique, and several types of Si-based micro-/nanohierarchical structures are successfully realized. The interaction effects of multiscale structures during the micro-/nanointegrated fabrication procedure is observed, including the interaction between microstructures and nanostructures and the influence of the MNHS geometry on the gold deposition. According to the optical property and liquid property measurements,

the fabricated Si-based MNHS materials show excellent anti-reflectance and super-hydrophobicity.

In summary, by experimental exploration, theoretical analysis, and mechanism investigation, we propose and realize a Si-based micro-/nanointegrated fabrication technique based on an improved DRIE process, which is cost-efficient, mass-fabrication, and wafer-level.

References

1. X.S. Zhang, Q.L. Di, F.Y. Zhu, G.Y. Sun, H.X. Zhang, Wideband anti-reflective micro/nano dual-scale structures: fabrication and optical properties. *Micro Nano Lett.* **6**, 947–950 (2011)
2. G. Sun, T. Gao, X. Zhao, H. Zhang, Fabrication of micro/nano dual-scale structures by improved deep reactive ion etching. *J. Micromech. Microeng.* **20**, 075028 (2010)
3. X.S. Zhang, F.Y. Zhu, G.Y. Sun, H.X. Zhang, Fabrication and characterization of squama-shape micro/nano multi-scale silicon material. *Sci. China E* **55**, 3395–3400 (2012)
4. X.S. Zhang, Q.L. Di, F.Y. Zhu, G.Y. Sun, H.X. Zhang, Superhydrophobic micro/nano dual-scale structures. *J. Nanosci. Nanotechnol.* **13**, 1539–1542 (2013)
5. X. Zhang, F. Shi, J. Niu, Y. Jiang, Z. Wang, Superhydrophobic surfaces: from structural control to functional application. *J. Mater. Chem.* **18**, 621–633 (2008)
6. N. Verplanck, Y. Coffinier, V. Thomy, R. Boukherroub, Wettability switching techniques on superhydrophobic surfaces. *Nanoscale Res. Lett.* **2**, 577–596 (2007)
7. L. Feng, Y. Song, J. Zhai, B. Liu, J. Xu, L. Jiang, D. Zhu, Creation of a superhydrophobic surface from an amphiphilic polymer. *Angew. Chem. Int. Ed.* **115**, 824–826 (2003)
8. A. Lafuma, D. Quéré, Superhydrophobic states. *Nat. Mater.* **2**, 457–460 (2003)
9. C. Lee, C.J. Kim, Maximizing the giant liquid slip on superhydrophobic microstructures by nanostructuring their sidewalls. *Langmuir* **25**, 12812–12818 (2009)
10. B.S. Kim, S. Shin, S.J. Shin, K.M. Kim, H.H. Cho, Micro-nano hybrid structures with manipulated wettability using a two-step silicon etching on a large area. *Nanoscale Res. Lett.* **6**, 333 (2011)
11. H. You, A.J. Steckl, Three-color electrowetting display device for electronic paper. *Appl. Phys. Lett.* **97**, 023514 (2010)
12. F. Mugele, J.C. Baret, Electrowetting: from basics to applications. *J. Phys. Condens. Matter* **17**, R705–R774 (2005)
13. W.C. Nelson, C.J. Kim, Monolithic fabrication of EWOD chips for picoliter droplets. *J. Microelectromech. Syst.* **20**, 1419–1427 (2011)

Micro/Nano Integrated Fabrication Technology and Its
Applications in Microenergy Harvesting

Zhang, X.-S.

2016, XX, 122 p. 95 illus., 76 illus. in color., Hardcover

ISBN: 978-3-662-48814-0